

# Simulation and optimization of triple cation Perovskite solar cell using SCAPS-1D

Ting Gou<sup>a</sup>, Yang Li<sup>a</sup>, Zeyuan Lv<sup>a</sup>, Minglin Zhao<sup>a,\*</sup>, Jun Dai<sup>a</sup>, Fuyang Cao<sup>b</sup>

<sup>a</sup> School of Science, Jiangsu University of Science and Technology, Zhenjiang 212100, PR China

<sup>b</sup> School of Materials Science and Engineering, Jiangsu University, Zhenjiang, 212013, PR China



## ARTICLE INFO

### Keywords:

Triple cation (Cs/FA/MA) perovskite solar cells  
Simulation  
SCAPS-1D  
Power conversion efficiency

## ABSTRACT

Triple cation ( $\text{Cs}_x(\text{MA}_{0.17}\text{FA}_{0.83})_{1-x}\text{Pb}(\text{I}_{0.83}\text{Br}_{0.17})_3$ ) perovskites have attracted extensive attention owing to their excellent stability and photovoltaic performance. In this work, an efficient perovskite solar cell with a structure of  $\text{TiO}_2/\text{Cs}_x(\text{MA}_{0.17}\text{FA}_{0.83})_{1-x}\text{Pb}(\text{I}_{0.83}\text{Br}_{0.17})_3$  ( $\text{CsFAMA}$ )/ $\text{CuSCN}$  was proposed and optimized theoretically using the solar cell simulator capacitance software (SCAPS-1D). This study optimized the parameters of the absorber layer, such as the thickness, doping density, defect density and bandgap. In addition, the electron transport layer (ETL) and the hole transport layer (HTL) are optimized by varying their electron affinity, thickness and doping density. It was found that the optimization of the absorber layer thickness and doping density provided a significant improvement in the efficiency of the device, while the parameters of both ETL and HTL showed minor influence on the device performance. Moreover, the operation temperature was discussed to provide further insight concerning the device performance. It showed that an increase of the operation temperature from 300 to 700 K resulted in reduction of device performance. And the  $\text{CsFAMA}$ -based device showed the highest power conversion efficiency (PCE) of 28.66% at 300 K with fill factor (FF) of 83.18%, open circuit voltage ( $V_{oc}$ ) of 1.48 V and short circuit current density ( $J_{sc}$ ) of  $23.27 \text{ mA/cm}^2$ . The optimized values of the absorber thickness, defect density and doping density were found to be 500 nm,  $2.6 \times 10^{13} \text{ cm}^{-3}$  and  $1 \times 10^{16} \text{ cm}^{-3}$ , respectively. The findings of this study suggest  $\text{CsFAMA}$ -based absorber materials can play an important role in high efficiency perovskite solar cells with excellent stability.

## 1. Introduction

Perovskite solar cells (PSCs), as the next-generation of low-cost and high-performance photovoltaic cells, have attracted significant attention due to their high absorption coefficients, long diffusion lengths, tunable bandgap, and high charge mobility [1–4]. Recently, the power conversion efficiency (PCE) of PSCs increased from 3.8% to 26.08% [5,6]. Currently, the biggest challenge of the mass-scale production of PSCs is their long-term stability. To date, many efforts have been made to improve the device performance of  $\text{MAPbI}_3$  (MA = methylammonium,  $\text{CH}_3\text{NH}_3^+$ ) based PSCs [7–10]. However, the moisture instability and thermal decomposition of MA cations limit the device's long-term stability [11]. More recently,  $\text{FAPbI}_3$  (FA = formamidinium,  $\text{CH}(\text{NH}_2)_2^+$ ) has attracted considerable interest owing to its excellent thermal stability [12]. However, the  $\text{FAPbI}_3$  tends to transform from photoactive  $\alpha$ -phase to non-perovskite

\* Corresponding author.

E-mail address: [zhaominglin@just.edu.cn](mailto:zhaominglin@just.edu.cn) (M. Zhao).

$\delta$ -phase under air ambient. Fortunately, an introduction of smaller cations, such as  $\text{MA}^+$  and  $\text{Cs}^+$ , into FA-based perovskite films can stabilize  $\alpha$ -phase and prevent the formation of  $\delta$ -phase [13]. Compared to binary cation perovskites ( $\text{CsFA}/\text{CsMA}/\text{MAFA}$ ), triple cation ( $\text{CsFAMA}$ ) perovskite exhibits a longer photoluminescence lifetime due to reduced defect density in the bandgap [14]. Therefore, the  $\text{CsFAMA}$  systems have gained increasing attentions in academia. S. Ašmontas et al. [15] reported that the PCE of the PSCs could reach up to 20.2% by using  $\text{Cs}_x(\text{MA}_{0.17}\text{FA}_{0.83})_{1-x}\text{Pb}(\text{I}_{0.83}\text{Br}_{0.17})_3$  as absorber with a Cs-doping density of 10%. While, A. M. El-Naggar et al. [16] reported that Cs-doped  $\text{MA}_{0.05}\text{FA}_{0.95}\text{Pb}(\text{I}_{0.98}\text{Br}_{0.02})_3$  films exhibited the highest PCE of 13.04%, when the films doped with 2% of Cs. M. Azam et al. [17] provided a highly-efficient PSC with PCE of 20.31% based on Cl incorporated triple cation perovskite materials ( $\text{Cs}_x\text{FA}_{0.2}\text{MA}_{0.8-x}\text{Pb}(\text{I}_{1-y}\text{Cl}_y)_3$ ). Nevertheless, the reported triple cation perovskites are limited, further studies are required to find an optimum triple cation perovskite-based PSCs with high efficiency and excellent stability.

Generally, it is costly and time-consuming to experimentally design PSCs, and the preparation process is harmful to the environment for the PSCs containing toxicants like Pb [18]. Numerical simulation provides a convenient and riskless way to explore the optimal parameters to obtain the optimized output of the PSCs [19]. The one-dimensional Solar Cell Capacitance Simulator (i. e. SCAPS-1D), which is based on solving the Poisson and the continuity equations [20], is one of the best simulating software. The SCAPS-1D simulator has been widely used in PSCs simulation [21–23]. It can carry out PSCs performance analysis with up to seven different layers in both bright and dark environments, and the stimulated results are in good agreement with experimental results.

In this work, we studied the photovoltaic (PV) performance of triple cation PSCs using SCAPS-1D. According to the existing experimental report [24], the triple cation perovskite  $\text{Cs}_x(\text{MA}_{0.17}\text{FA}_{0.83})_{1-x}\text{Pb}(\text{I}_{0.83}\text{Br}_{0.17})_3$  was selected as absorber layer. Except for the absorber layer, the choice of the hole transport layer (HTL) and the electron transport layer (ETL) are also of vital importance to optimize the device performance. To date, Spiro-OMeTAD is the most commonly used HTL, which could significantly improve the PCE. However, it is unstable and exhibits low hole mobility in pristine form [25]. Copper thiocyanate (CuSCN) possesses excellent hole mobility ( $0.1 \text{ cm}^2\text{V}^{-1}\text{s}^{-1}$ ) and exhibits a higher stability with dopants [26]. M. Jung et al. [27] found that, compared to Spiro-OMeTAD, using CuSCN as HTL could achieve higher efficiency and improved thermal stability. By employing CuSCN, S. Ye et al. [28] have successfully fabricated  $\text{MAPbI}_3$ -based PSCs with a highest PCE of 16.6%. J. W. Jung et al. [29] demonstrated that CuSCN is an outstanding HTL for high-performance thin-film planar heterojunction PSCs. The high optical transparency of CuSCN over the visible range makes it a good choice for tandem structures as well [29]. Furthermore, CuSCN can effectively reduce the charge recombination loss at the HTL/perovskite interface [26]. Most importantly, CuSCN possesses favorable energy levels ( $E_{VB} = -5.3 \text{ eV}$ , VB = valence band), whose VB is just slightly higher than that of the CsFAMA absorber layer. Hence, CuSCN was chosen as the proper HTL. In addition, Titanium dioxide ( $\text{TiO}_2$ ) is chosen as the ETL. As the most used ETL for PSCs,  $\text{TiO}_2$  is developed by J. Choi et al. [30] in 2016, which was found to be able to provide outstanding electron extraction and hole blocking in a planar PSC. In addition, the band alignment between  $\text{TiO}_2$  and CsFAMA is conducive to electron transport [31].

In this paper, we use SCPAS-1D simulator to conduct extensive study of CsFAMA-based PSCs with  $\text{TiO}_2$ , CuSCN and triple cation  $\text{Cs}_x(\text{MA}_{0.17}\text{FA}_{0.83})_{1-x}\text{Pb}(\text{I}_{0.83}\text{Br}_{0.17})_3$  as ETL, HTL and absorber layer, respectively. The thickness, doping density, defect density and bandgap of the absorber layer, as well as the electron affinity, thickness and doping density of both ETL and HTL were optimized through device simulation. Furthermore, the influence of the operation temperature is also explored. The numerical simulation results of this study will provide helpful guidance to the experimental studies of CsFAMA-based PSCs with high efficiency and excellent stability.

## 2. Device simulation Details

The simulation was carried out using SCAPS-1D, which is developed by University of Gent, Belgium [32]. It is often used to simulate the PV performance of solar cells. The carrier band distribution, electric field distribution and J-V characteristics of the device can be simulated based on three basic equations, namely, Poisson's equation and Continuity equations [32]:

$$\frac{d}{dx} \left( \epsilon_r \frac{d\Psi}{dx} \right) = -q(p(x) - n(x) + N_D^+ - N_A^- + p_t - n_t) \quad (1)$$

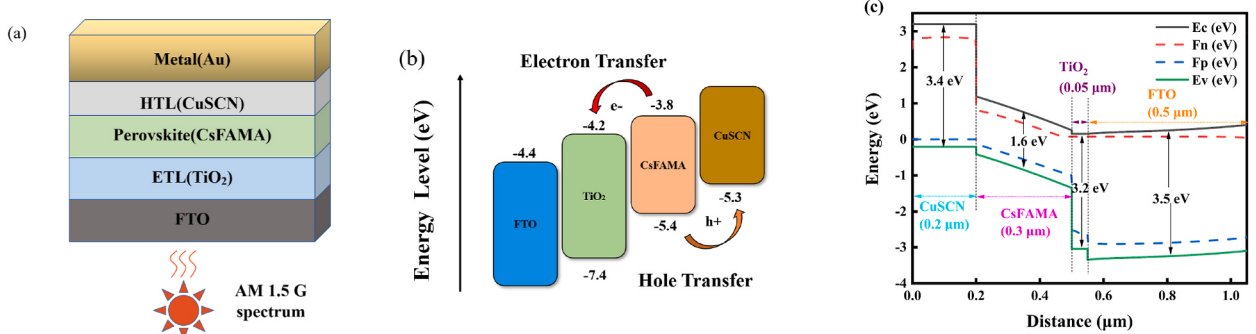


Fig. 1. (a) The schematics of device structure for simulations (b) Energy band diagram and (c) the grading of energy.

$$\frac{dJ_n}{dx} = q(R_n - G_n) \quad (2)$$

$$\frac{dJ_p}{dx} = q(G_p - R_p) \quad (3)$$

where  $\psi$  denotes the electrostatic potential energy,  $\epsilon_r$  is relative permittivity,  $q$  is electron charge,  $n$  is electron density,  $p$  is hole density,  $p_t$  is trapped hole,  $n_t$  is trapped electrons,  $N_A$  is the ionized acceptor density,  $N_D$  is the ionized donor density,  $J_n/J_p$  are electron/hole current density,  $G_n/G_p$  are the generation rate of electrons/holes,  $R_n/R_p$  are the electron/hole recombination rate.

The triple cation PSC device is simulated with the device structure of Fluorine doped tin oxide (FTO)/TiO<sub>2</sub>/Cs<sub>x</sub>(MA<sub>0.17</sub>FA<sub>0.83</sub>)<sub>1-x</sub>Pb(I<sub>0.83</sub>Br<sub>0.17</sub>)<sub>3</sub>/CuSCN/Au, as shown in Fig. 1 (a). FTO was applied as the front contact glass, TiO<sub>2</sub> was employed as the ETL, triple cation CsFAMA perovskite material was used as the absorber layer, CuSCN was used as the HTL, and Au was used as the metal rear contact. Fig. 1 (b) and Fig. 1 (c) show the energy band level structure and the grading energy of the device, respectively. The VB of the CsFAMA is just slightly higher than that of TiO<sub>2</sub> and lower than that of CuSCN. This ideal band alignment is desired for PSC structure.

For simulation, standard AM1.5G spectra with 1000 W/m<sup>2</sup> was used, and the operation temperature is 300 K. The thickness, doping density, defect density, etc. of each layer are examined, for these parameters have great impact on morphology, electrical properties and optical properties of the materials [33]. The variation of electron affinity of both ETL and HTL is investigated to study the influence of conduction band offset (CBO) for CsFAMA/TiO<sub>2</sub> interface and valence band offset (VBO) for CuSCN/CsFAMA interface. The interface defect density of the two interfaces are also taken into consideration. In the SCAPS-1D simulation, the input parameters are provided in Table 1. The defect density introduced at each of the CsFAMA/TiO<sub>2</sub> and CuSCN/CsFAMA interfaces are summarized in Table 2. These parameters were adopted from multiple theories and literatures [23,33–37]. With the development of technology and the widened application scenarios, the operation temperature has no longer been confined to room temperature. Thus, the influence of operation temperature on solar cell performance is also investigated. The PV parameters that can be measured by the SCAPS-1D software, are power conversion efficiency (PCE), fill factor (FF), short circuit current ( $J_{sc}$ ), and open circuit voltage ( $V_{oc}$ ). The initial calculated parameters are as follows: PCE = 21.31%, FF = 79.41%,  $J_{sc}$  = 19.00 mA/cm<sup>2</sup>,  $V_{oc}$  = 1.41 V. Comparison of our simulation results with previously published experimental results, in terms of  $V_{oc}$ ,  $J_{sc}$ , FF and PCE for the triple cations PSC device, are provided in Table 3 [38]. Our simulation results are comparable to the experimental results, suggesting the reliability of our simulation. The difference between our simulation results and the reference experimental results might be derived from the difference in absorber layer thickness, FTO and Au layers.

### 3. Results and discussion

#### 3.1. Optimization of the thickness of absorber layer

The thickness of the perovskite absorber layer plays a significant role in determining the device performance. It is well known that the absorber thickness could affect the diffusion length and the carriers lifetime [39]. Thus, we have varied the thickness of the CsFAMA absorber layer from 100 nm to 1000 nm to investigate the effect of absorber thickness and obtain the optimal thickness value. Fig. 2 (a) displays the current density-voltage (J-V) curve for different absorber thickness. Fig. 2 (b) shows the variation of FF and PCE for the triple cations PSC device as a function of the absorber thickness.

With increasing absorber layer thickness,  $J_{sc}$  increases rapidly within 500 nm, and then  $J_{sc}$  is almost unchanged. A large absorption coefficient of the perovskite is the reason for increased  $J_{sc}$ . While, when the absorber thickness reaches a certain value, the photon absorption reaches saturation due to the recombination of the generated charge carriers [40]. With increasing absorber layer thickness,  $V_{oc}$  remains almost constant. As shown in Fig. 2 (b), it can be observed that PCE exhibits similar nature to that of  $J_{sc}$ . While, FF decreases from 81.68% to 75.97% with respect to the absorber layer thickness. The FF decreases monotonously with increasing absorber thickness, which may be attributed to an increase in series resistance [41]. The phenomenon observed in this study is in agreement with previous studies [42–45]. The optimal thickness for optical absorption and carrier collection is contrary to one another in the simulation of PSCs. To balance the two factors, the optimal thickness of perovskite absorber is determined to be 500 nm for further

**Table 1**  
SCAPS input parameters for the CsFAMA-based PSC device.

	TiO <sub>2</sub>	CsFAMA	CuSCN	FTO
Thickness (nm)	50	300	200	500
Bandgap E <sub>g</sub> (eV)	3.2	1.6	3.4	3.5
Electron affinity $\chi$ (eV)	4	3.9	1.9	4
Dielectric permittivity $\epsilon_r$	100	6.5	10	9
Conduction band density of states N <sub>C</sub> (cm <sup>-3</sup> )	10 <sup>21</sup>	10 <sup>17</sup>	1.7 × 10 <sup>19</sup>	2.2 × 10 <sup>17</sup>
Valence band density of states N <sub>V</sub> (cm <sup>-3</sup> )	2 × 10 <sup>20</sup>	10 <sup>17</sup>	2.5 × 10 <sup>21</sup>	2.2 × 10 <sup>16</sup>
Electron mobility $\mu_e$ (cm <sup>2</sup> V <sup>-1</sup> s <sup>-1</sup> )	6 × 10 <sup>-3</sup>	2	10 <sup>-4</sup>	20
Hole mobility $\mu_p$ (cm <sup>2</sup> V <sup>-1</sup> s <sup>-1</sup> )	6 × 10 <sup>-3</sup>	2	0.1	10
Donor density N <sub>D</sub> (cm <sup>-3</sup> )	5 × 10 <sup>19</sup>	0	0	1 × 10 <sup>15</sup>
Acceptor density N <sub>A</sub> (cm <sup>-3</sup> )	0	10 <sup>13</sup>	1 × 10 <sup>18</sup>	0
Total defect density N <sub>t</sub> (cm <sup>-3</sup> )	1 × 10 <sup>14</sup>	2.6 × 10 <sup>13</sup>	2 × 10 <sup>14</sup>	1 × 10 <sup>15</sup>

**Table 2**

SCAPS input parameters of interface defect layers.

interface	CsFAMA/TiO <sub>2</sub>	CuSCN/CsFAMA
Defect type	neutral	neutral
Capture Cross Section: Electrons/holes	$1 \times 10^{-19}/1 \times 10^{-19}$	$1 \times 10^{-19}/1 \times 10^{-19}$
Energetic Distribution	Single	Single
Reference for defect energy level	Above the highest EV	Above the highest EV
Total density (cm <sup>-3</sup> ) (integrated over all energies)	$1 \times 10^9$	$1 \times 10^{10}$

**Table 3**

Comparison of PV parameters of our initial simulation and the reference experimental results [38].

	V <sub>oc</sub> (V)	J <sub>sc</sub> (mA/cm <sup>2</sup> )	FF (%)	PCE (%)
Experimental	1.103	23.39	76.1	20.03
Initial simulation	1.41	19.00	79.41	21.31

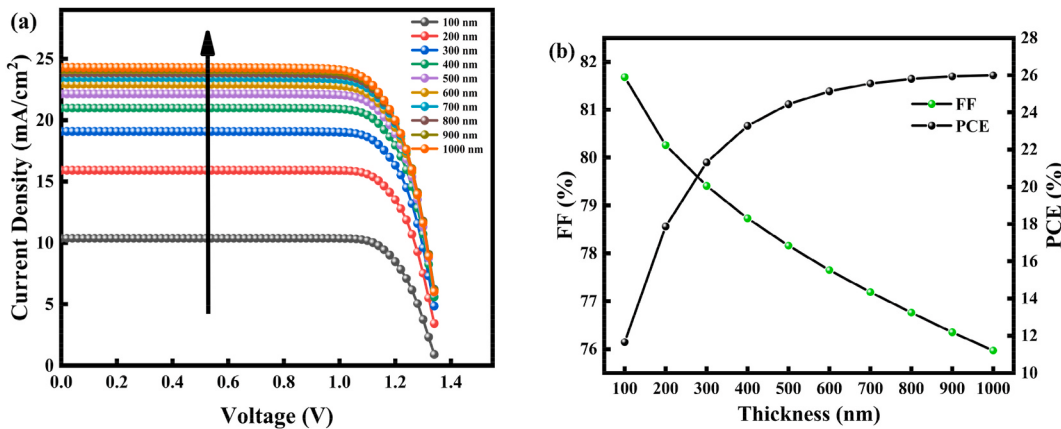


Fig. 2. Effect of variation of CsFAMA absorber thickness on the performance of the device, (a) J-V curve (b) PCE and FF.

simulation. The device performance is as follows: PCE = 24.44%, FF = 78.16%,  $J_{sc} = 22.07$  mA/cm<sup>2</sup>,  $V_{oc} = 1.42$  V.

### 3.2. Optimization of acceptor density of absorber layer

For CsFAMA perovskite demonstrating a p-type behavior, the acceptor density ( $N_A$ ) of the absorber layer was varied from  $1 \times 10^{13}$  cm<sup>-3</sup> to  $1 \times 10^{17}$  cm<sup>-3</sup> to understand how  $N_A$  affecting the PV parameters. The J-V characteristics for each  $N_A$  are shown in Fig. 3 (a), and the fluctuation of FF and PCE vs  $N_A$  is shown in Fig. 3 (b). The values of  $J_{sc}$  and  $V_{oc}$  stay nearly constant up to  $1 \times 10^{16}$  cm<sup>-3</sup>. When

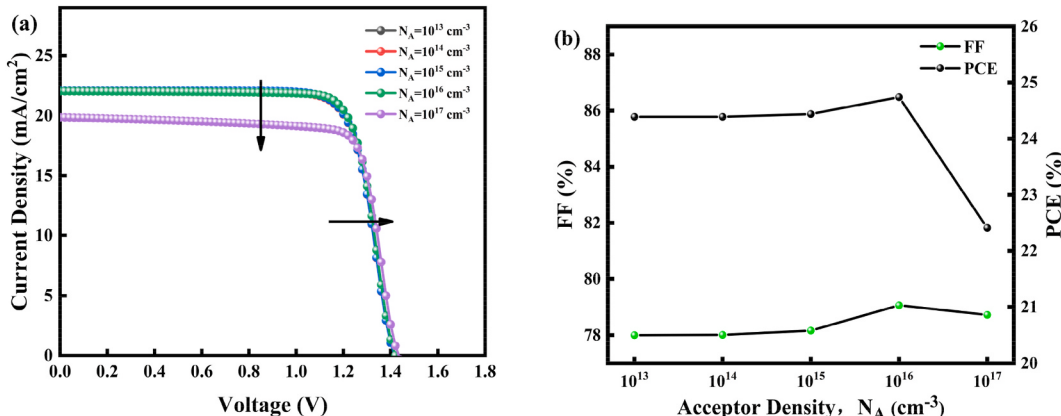


Fig. 3. Effect of variation of CsFAMA absorber acceptor density on the performance of the device (a) J-V curve (b) PCE and FF.

the  $N_A$  increases till  $1 \times 10^{17} \text{ cm}^{-3}$ , the  $J_{sc}$  decreases, and the  $V_{oc}$  increases. With increasing  $N_A$ , the Fermi energy level of the holes decreases and approaches the VB, resulting in an increase of  $V_{oc}$  [21]. In addition, an increase in  $N_A$  enhances the built-in electric field which further promotes the separation of the generated charge carriers, resulting in an increase in  $V_{oc}$  [40]. Moreover, the PCE drops rapidly when  $N_A$  exceeds  $1 \times 10^{16} \text{ cm}^{-3}$ , which could be attributed to the enhanced Auger recombination and charge-carrier recombination [41]. As such, the value of  $N_A$  is chosen to be  $1 \times 10^{16} \text{ cm}^{-3}$  for further simulation.

### 3.3. Optimization of defect density of absorber layer

Apart from thickness and acceptor density, the defect density ( $N_t$ ) of absorber layer is also important to the device performance. The perovskite absorber layer contains different defects such as interstitials, vacancies, Schottky and Frenkel defects [41]. These bulk defects directly influence the perovskite properties and facilitate nonradiative electron-hole recombination [46]. Except for bulk defects, interfacial defects originated from structural mismatch or environment impurities, could lead to the recombination of electron-hole pairs as well [47]. In this section, we have taken the interfacial defects into account. On top of that, the  $N_t$  of absorber layer were varied from  $2.6 \times 10^{11} \text{ cm}^{-3}$  to  $2.6 \times 10^{18} \text{ cm}^{-3}$  to obtain the impact of  $N_t$  over the PV parameters of the device. The obtained results are present in Fig. 4. It is found that the PV parameters of the device decreases slightly when  $N_t$  values varying from  $2.6 \times 10^{11} \text{ cm}^{-3}$  to  $2.6 \times 10^{14} \text{ cm}^{-3}$ . Then, the degradation of these PV parameters turns to be obvious when  $N_t$  exceeds  $2.6 \times 10^{14} \text{ cm}^{-3}$ . This is possibly attributed to a higher rate of recombination. In other words, the diffusion length of electrons and holes may be reduced with increasing  $N_t$  values, which harms the device performance [48]. Consequently, lower  $N_t$  values provides excellent device performance. However, it is impractical to achieve a very low  $N_t$  in any materials. Therefore, in this manuscript, the value of  $N_t$  is predicted to be  $2.6 \times 10^{13} \text{ cm}^{-3}$  for further simulation.

### 3.4. Optimization of bandgap of absorber layer

The bandgap ( $E_g$ ) of absorber layer directly influences the PV parameters of the device, for it can directly affect the ability of PSCs to capture light [33]. As reported previously [49], the bandgap of CsFAMA perovskite, obtained by experiments, is within the range from 1.56 eV to 1.70 eV. Thus, we chose the above-mentioned bandgap range for following simulation. Fig. 5 shows the response of the PV parameters vs  $E_g$  of absorber layer. It can be seen that the  $J_{sc}$ , FF and PCE decrease, only the  $V_{oc}$  increases. When the  $E_g$  raises, the conduction band offset decreases, which enhances the carrier generation and promotes the exciton segregation [50], thereby

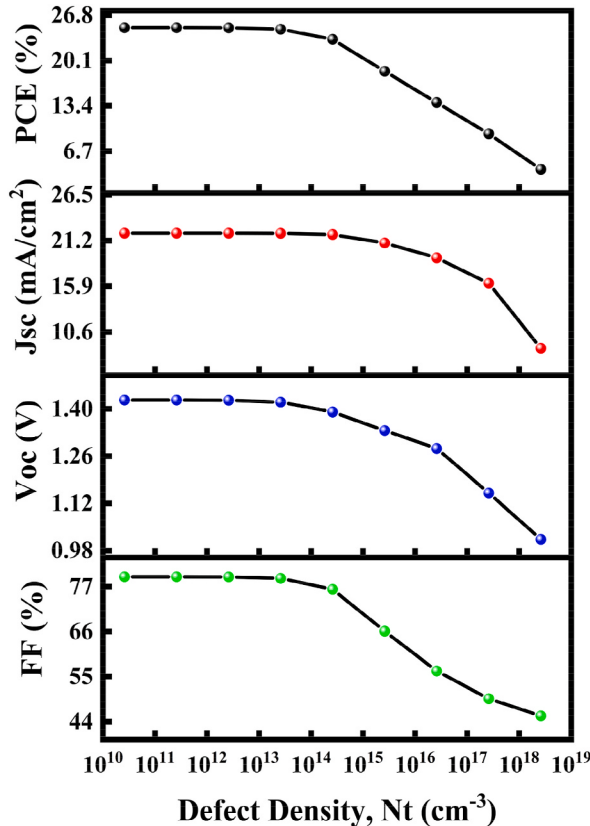


Fig. 4. Effect of variation of CsFAMA absorber defect density on the performance of the device.

increasing  $V_{oc}$ . The reduction of the  $J_{sc}$  with increasing  $E_g$  can be attributed to hindered absorption of photons [51]. For the high bandgap of CsFAMA perovskite restricts the device efficiency, the optimal value of  $E_g$  is chosen as 1.56 eV, with  $V_{oc} = 1.41$  V,  $J_{sc} = 23.25$  mA/cm<sup>2</sup>, FF = 79.43%, PCE = 26.13%.

### 3.5. Optimization of thickness and doping density of ETL and HTL

The ETL and HTL are important components of the structure of PSCs. ETL can improve the transmission of electrons by decreasing electron-hole recombination and blocking photogenerated holes [23]. HTL can collect holes from the absorber layer and transfer them to the metal contact [52]. The thickness of ETL and HTL have great impact on the device stability and performance. Moreover, the doping density of ETL and HTL significantly affect the PSCs' performance. Doping density variation influences the device performance via built-in electric field, which would increase with increasing doping density. The enhanced built-in electric field will lead to high exciton dissociation and high carrier mobility with less recombination rate [46]. Additionally, appropriate doping density can enhance the interface potential and reduce interface recombination, thus improving the device performance [22].

In this work, the n-type TiO<sub>2</sub> was used as ETL, the thickness of ETL was varied from 30 nm to 100 nm, and the doping density of ETL was varied from  $5 \times 10^{13}$  cm<sup>-3</sup> to  $5 \times 10^{20}$  cm<sup>-3</sup> for the simulation. The variation of thickness and doping density of ETL layer and the response of PV parameters are present in Fig. 6. It can be seen that the PSC has minimal PV performance fluctuation with ETL thickness variation. According to the fact that too thick ETL layer will lead to additional resistance and raise the recombination rate, while too thin ETL layer cannot effectively block the holes [30]. The optimal ETL thickness is selected as 40 nm. As shown in Fig. 6, the  $V_{oc}$ , FF and PCE of the device performance increase significantly with the doping density arrived to  $5 \times 10^{20}$  cm<sup>-3</sup>, while the  $J_{sc}$  decreases slightly with the doping density raised up to  $5 \times 10^{20}$  cm<sup>-3</sup>. Apart from the above explanation, this phenomenon also related to the fact that an increasing doping density could reduce ohmic losses in transport layer and improve the conductivity [53]. Thus, we considered the ETL's optimal doping density to be  $5 \times 10^{20}$  cm<sup>-3</sup> for further simulation.

CuSCN, which exhibits intrinsic p-type conductivity, was selected as the HTL layer in this work. The HTL thickness was varied from 50 nm to 350 nm, and the doping density was varied from  $1 \times 10^{13}$  cm<sup>-3</sup> to  $1 \times 10^{20}$  cm<sup>-3</sup>. The obtained PV parameters consist of  $V_{oc}$ , FF,  $J_{sc}$  and PCE are present in Fig. 7. The results reveal that HTL thickness has minor influence on the device performance. Considering that thinner HTL would allow more light to be transmitted to the absorber layer, a thickness of 200 nm was chosen for the simulation. Contrary to the thickness, the variation of doping density has a considerable impact on the PV parameters. In accordance with Fig. 7, the PV parameters initially increase slowly up to  $1 \times 10^{19}$  cm<sup>-3</sup>, then these parameters increase quickly up to  $1 \times 10^{20}$  cm<sup>-3</sup>. As

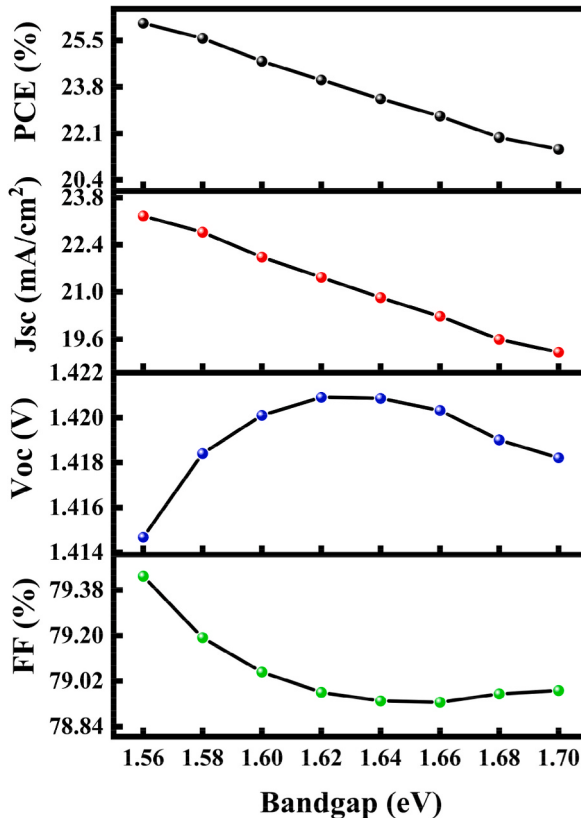


**Fig. 5.** Effect of variation of CsFAMA bandgap on the performance of the device.

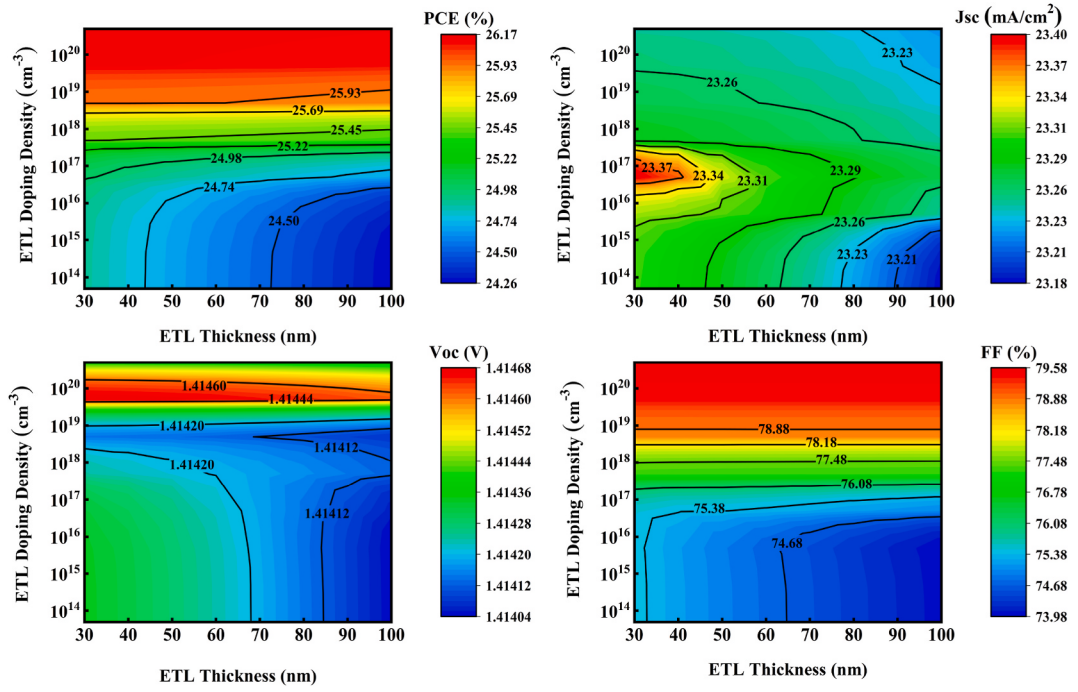


**Fig. 6.** Effect of variation of ETL thickness and doping density on the performance of the device.

mentioned above, the improvement of the device performance could be attributed to the enhancement of the built-in electric field. Thus, HTL doping density was set to be  $1 \times 10^{20} \text{ cm}^{-3}$  for further simulation.

### 3.6. Optimization of electron affinity of ETL and HTL

The electron affinity ( $\chi$ ) of ETL and HTL plays an important role in study of the efficiency of PSC, because they create interfaces for

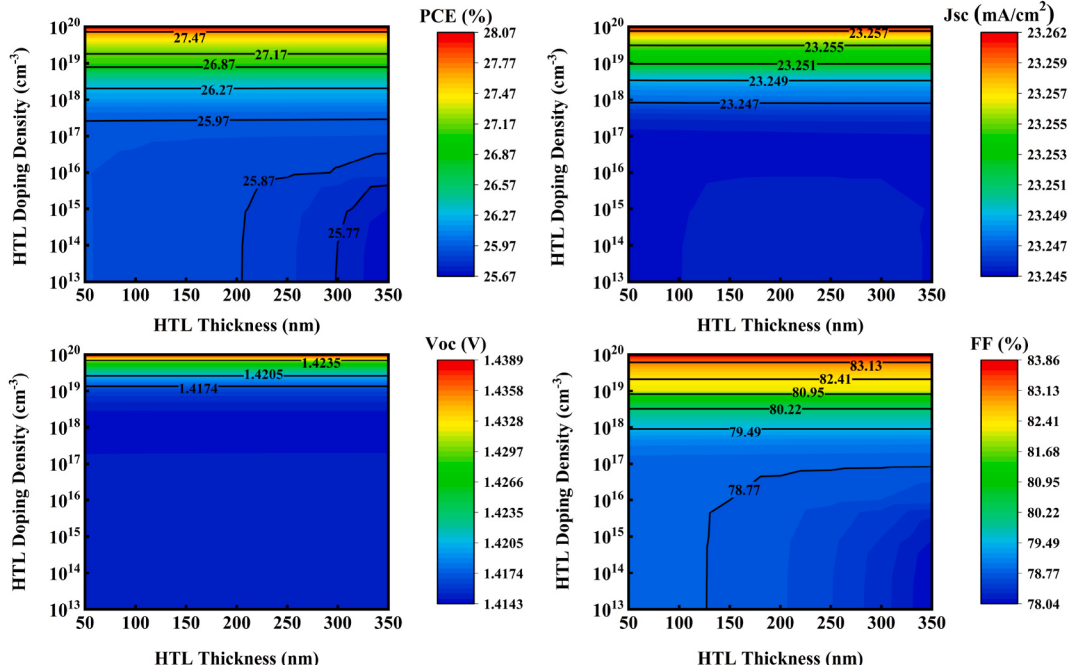


**Fig. 7.** Effect of variation of HTL thickness and doping density on the performance of the device.

charge transport. Considering the CBO for the CsFAMA/TiO<sub>2</sub> interface and the VBO for the CuSCN/CsFAMA interface, the optimized  $\chi$  can be obtained [54].

$$CBO = \chi_{\text{absorber}} - \chi_{\text{ETL}} \quad (4)$$

$$VBO = (\chi_{\text{HTL}} + E_{g-\text{HTL}}) - (\chi_{\text{absorber}} + E_{g-\text{absorber}}) \quad (5)$$

where  $\chi_{\text{absorber}}$ ,  $\chi_{\text{ETL}}$  and  $\chi_{\text{HTL}}$  are the electron affinity of absorber layer, ETL and HTL, respectively.  $E_{g-\text{absorber}}$  and  $E_{g-\text{HTL}}$  are the bandgap of absorber layer and HTL, respectively. In the following simulations,  $\chi$  of absorber layer and the bandgap of each layer were always kept constant. To investigate the impact of  $\chi$  of the ETL on the device performance,  $\chi$  of the ETL was adjusted from 3.7 eV to 4.3 eV, while  $\chi$  of HTL was fixed at 1.9 eV. The observed trends in  $V_{\text{oc}}$ , FF,  $J_{\text{sc}}$  and PCE are shown in Fig. 8(a). It can be seen that all of these parameters almost keep constant up to 3.9 eV. While, in the range of 3.9 eV–4.3 eV, the  $V_{\text{oc}}$ , FF and PCE decrease and the  $J_{\text{sc}}$  increases. The CBO at the CsFAMA/TiO<sub>2</sub> interface regulates the transmission of carriers through the contact. The CBO decreases with increasing  $\chi$  of the ETL. The too low CBO indicates the energy-level mismatch between the absorber layer and the ETL for electron transport, which may lead to an increase of electron-hole recombination [55]. As shown in Fig. 9 (a), when the electron affinity energy of ETL is 3.7 eV, a spike-like structure is formed at the CsFAMA/TiO<sub>2</sub> interface ( $CBO = +0.2$  eV). While, with increasing  $\chi$  of the ETL, the spike structure turns into cliff structure ( $CBO = -0.4$  eV). The formation of cliff at the interface will cause carriers back-transfer to the absorber layer, enhancing the electron-hole recombination. In addition, the blocked electrons located at the cliff-type interface will further reduce the electric field. All these factors lead to a decrease in device performance. Thereby, the optimal value of  $\chi$  is chosen as 3.7 eV.

In terms of HTL, it can be seen from Fig. 8(b) that  $V_{\text{oc}}$ ,  $J_{\text{sc}}$  and PCE increase when  $\chi$  of the HTL increased from 1.7 eV to 2.1 eV. However, the change in FF was more complex. The FF first increased from 81.82% to 83.90% in the range of 1.7 eV–1.9 eV, and then decreased to 82.96% at 2.0 eV, finally reached 83.18% at 2.1 eV. The VBO for CuSCN/CsFAMA interface varied from negative to positive (from  $-0.36$  eV to  $+0.04$  eV) with an increase of  $\chi$  of the HTL. As shown in Fig. 9(b), the corresponding band diagram at CuSCN/CsFAMA interface is changed from cliff-type into spike-type. It has been reported that the spike could enhance the built-in electric field and cause a lower interfacial recombination, resulting in high  $V_{\text{oc}}$  [56]. In addition, the spike will lead to a higher charge accumulation at the interface, which causes the formation of excess electrostatic potential, contributing to the increase of  $V_{\text{oc}}$  [57]. As PCE is a function of  $V_{\text{oc}}$ ,  $J_{\text{sc}}$  and FF, we have set the optimal  $\chi_{\text{HTL}}$  as 2.1 eV to achieve the positive VBO with the optimum PCE. The best device performance is as follows:  $V_{\text{oc}} = 1.48$  V,  $J_{\text{sc}} = 23.27$  mA/cm<sup>2</sup>, FF = 83.18%, PCE = 28.66%.

### 3.7. Optimization of device operation temperature

PSCs are sensitive to operation temperature, in general, increasing operation temperature has a negative effect on the device performance. The operation temperature for PSCs is usually at 300 K. However, for special application scenarios such as space, higher

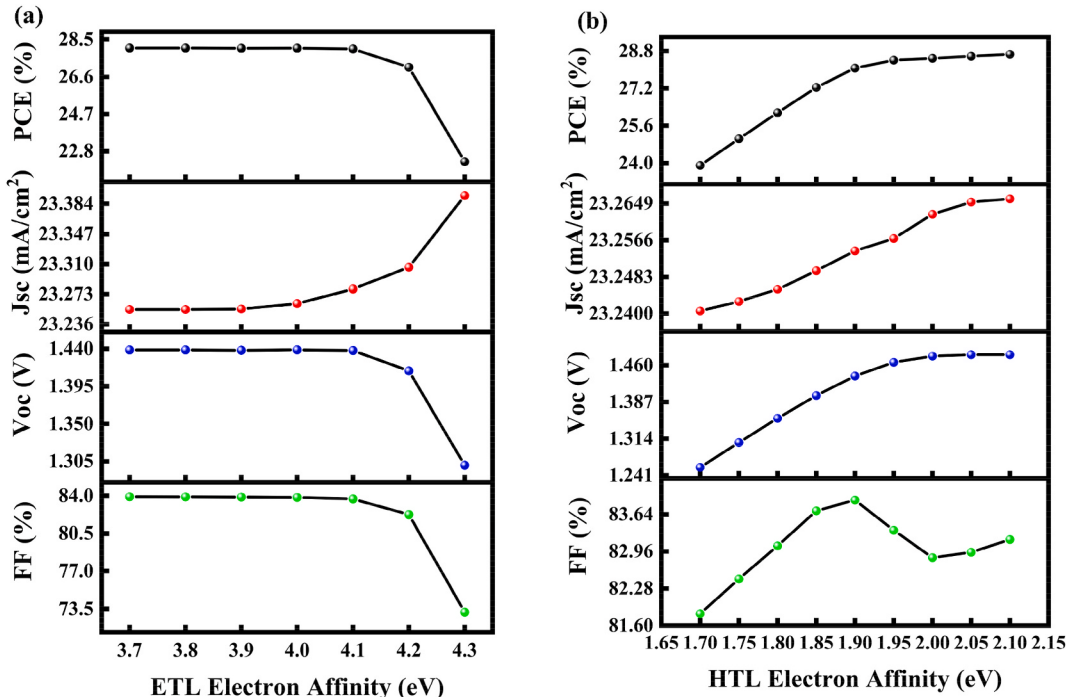


Fig. 8. Effect of variation of the electron affinity of (a) ETL and (b) HTL on the performance of the device.

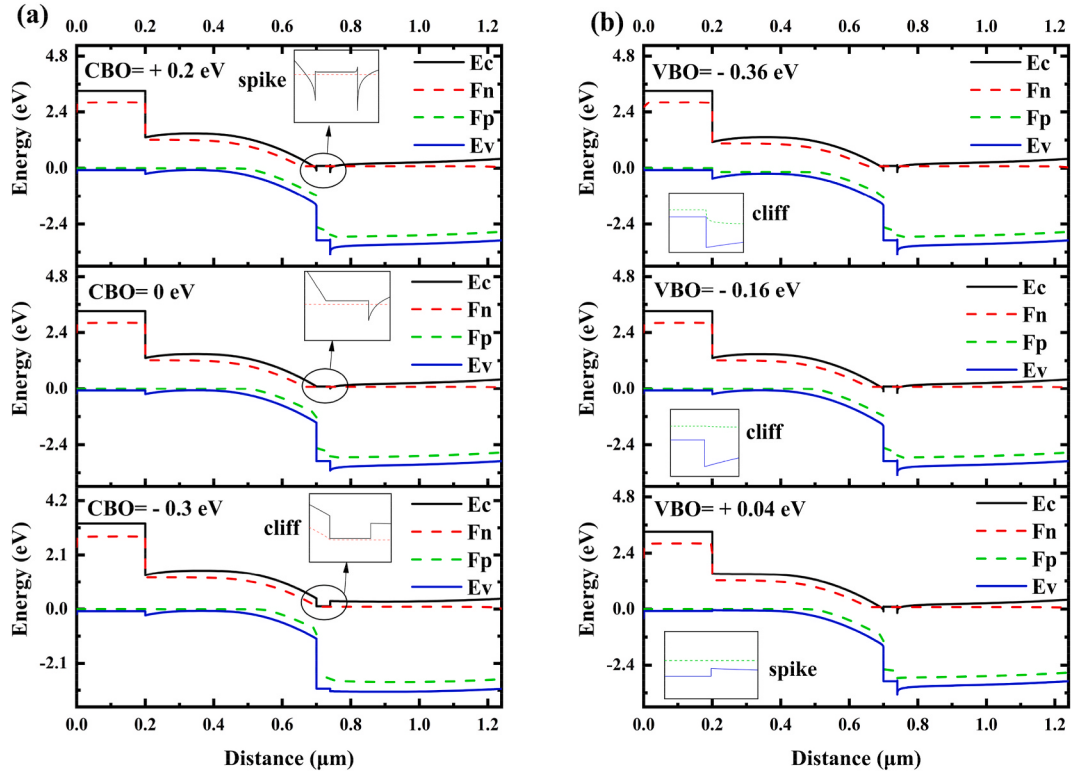


Fig. 9. Energy band diagrams of PSCs with different (a) CBO and (b) VBO.

operation temperature is required. It is of great significance to investigate the effect of operation temperature on the stability of the device performance. In this manuscript, CsFAMA perovskite device exhibits excellent thermal stability, therefore the operation temperature is altered from 300 K to 700 K. Fig. 10 (a) shows the PV parameters as a function of operation temperature, and Fig. 10 (b) exhibits the J-V curves vs operation temperature. The results show that  $V_{oc}$ , FF and PCE decrease with increasing operation temperature, while  $J_{sc}$  slightly increases. Similar to the discussion of absorber bandgap, an increase in temperature causes a reduction in  $E_g$ , resulting in the generation of additional charge carriers and consequently increased  $J_{sc}$  [45,51]. As for  $V_{oc}$ , the reduction of  $E_g$  and the enhancement of carrier concentrations will lead to an increase in the reverse saturation current density and consequently decreased  $V_{oc}$  [58]. In addition, high temperature raises the defects and narrows the bandgap, resulting in an increase in electron-hole recombination rate. The diffusion lengths  $L_D$  is defined as  $L_D = \sqrt{D/R_{total}}$ , here D is the diffusion constant,  $R_{total}$  is the total recombination rate, including radiative, auger and SRH recombination [59]. Thus, the enhanced  $R_{total}$  shortens the charge carrier diffusion length, resulting in a lower  $V_{oc}$ . The similar phenomenon has also been observed in previous literatures [43,44,60–62]. As shown in Fig. 10 (b), the operation temperature has a great impact on  $V_{oc}$ , which is responsible for the degradation of the overall device performance. Therefore, the optimal operation temperature of the device is 300 K.

### 3.8. Analysis of final optimized results

Finally, the optimal performance of the solar cell with the structure of FTO/CuSCN/Cs<sub>x</sub>(MA<sub>0.17</sub>FA<sub>0.83</sub>)<sub>1-x</sub>Pb(I<sub>0.83</sub>Br<sub>0.17</sub>)<sub>3</sub>/TiO<sub>2</sub>/Au was obtained based on the above optimized input parameters via SCAPS-1D software. Fig. 11 shows the J-V curves of the device before and after optimization. It can be seen that the J-V characteristic of the device has been significantly improved, demonstrating up to 28.66% of PCE, 23.27 mA/cm<sup>2</sup> of  $J_{sc}$ , 1.48 V of  $V_{oc}$ , and 83.18% of FF. Table 4 presents the comparison of our simulation results with other published results. Clearly, the FTO/TiO<sub>2</sub>/Perovskites/CuSCN/Metal structure proposed in this study exhibits the highest PCE. In this work, the above-mentioned structure is adopted to construct the triple cation PSC. By performing SCAPS simulation on this structure, a high efficiency perovskite solar cell with excellent stability can be achieved.

## 4. Conclusion

In this work, we studied the PSCs with the structure of TiO<sub>2</sub>/Cs<sub>x</sub>(MA<sub>0.17</sub>FA<sub>0.83</sub>)<sub>1-x</sub>Pb(I<sub>0.83</sub>Br<sub>0.17</sub>)<sub>3</sub>/CuSCN using SCAPS-1D simulation. The PSC design was based on the excellent stability of the triple cation perovskite and CuSCN. Basic parameters including thickness, doping density of the absorber layer, ETL and HTL, together with the defect density and bandgap of the absorber layer, and the electron affinity of both ETL and HTL, were investigated to achieve optimal device performance. The results showed that the device

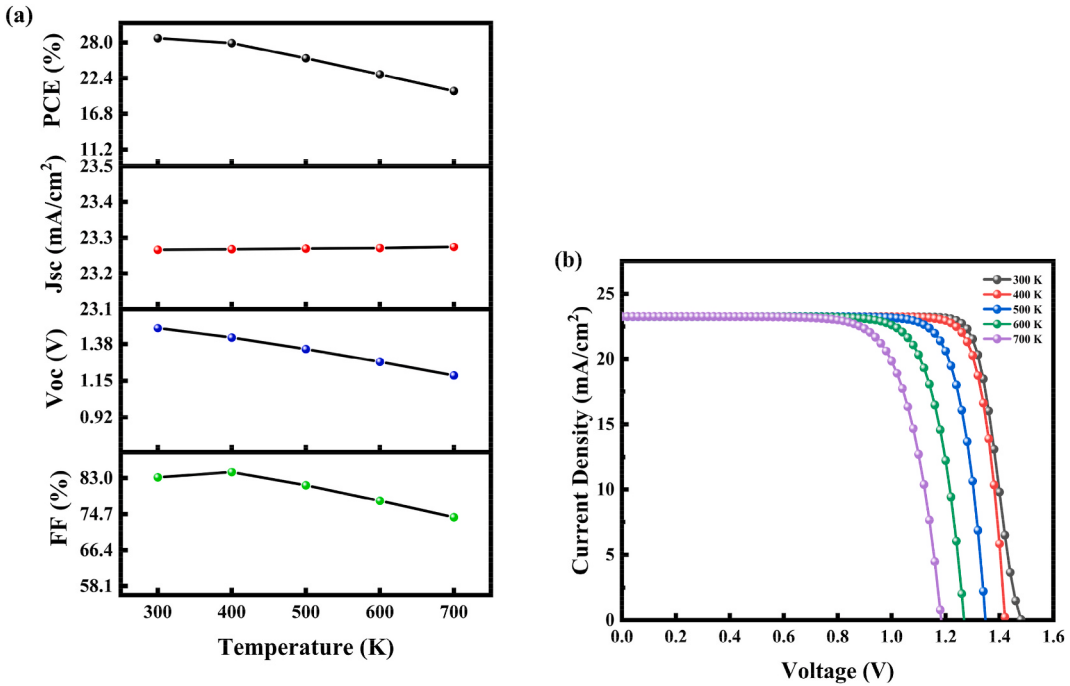


**Fig. 10.** Effect of variation of operation temperature on (a) the performance of PSC and (b) J-V curve.

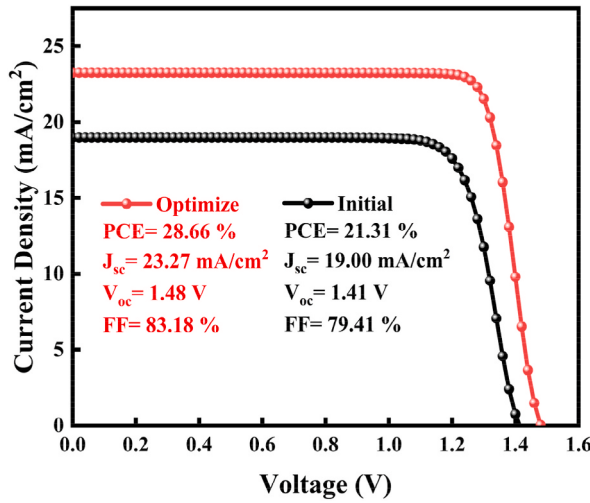


**Fig. 11.** Comparison of J-V curves.

**Table 4**

The device performance comparison of our results and other published results.

Device structure	$V_{oc}$ (V)	$J_{sc}$ (mA/cm <sup>2</sup> )	FF (%)	PCE (%)	Methodology	Ref.
FTO/ZnO/CsPbI <sub>3</sub> /CuSbS <sub>2</sub> /Se	1.10	16.44	62.64	15.6	Simulation	[58]
FTO/c-TiO <sub>2</sub> /m-TiO <sub>2</sub> /MAPbI <sub>3</sub> /Spiro-OMeTAD/Au	1.21	22.51	74.39	20.26	Simulation	[63]
FTO/SnO <sub>2</sub> /FAPbI <sub>3</sub> /Spiro-OMeTAD/Au	1.2	22.6	77	21.4	Simulation	[64]
FTO/SnO <sub>2</sub> /FA <sub>0.85</sub> Cs <sub>0.15</sub> PbI <sub>3</sub> /Spiro-OMeTAD/Au	1.2	21.5	78	21.0	Simulation	[64]
FTO/SnO <sub>2</sub> /FA <sub>0.85</sub> Cs <sub>0.15</sub> Pb(I <sub>0.85</sub> Br <sub>0.15</sub> ) <sub>3</sub> /Spiro-OMeTAD/Au	1.3	20.2	72	18.7	Simulation	[64]
FTO/CdS/MAPbI <sub>3-x</sub> Cl <sub>x</sub> /PCBM/Au	1.2	27	85	26.6	Simulation	[48]
FTO/TiO <sub>2</sub> /MAPbI <sub>3</sub> /CuSCN/Ni	1.1	28.9	82.08	28.9	Simulation	[23]
FTO/TiO <sub>2</sub> /CsFAMAPbI <sub>3-x</sub> Br <sub>x</sub> /CuSCN/Au	1.103	23.39	76.1	20.03	Experimental	[38]
FTO/TiO <sub>2</sub> /Cs <sub>x</sub> (MA <sub>0.17</sub> FA <sub>0.83</sub> ) <sub>1-x</sub> Pb(I <sub>0.83</sub> Br <sub>0.17</sub> ) <sub>3</sub> /CuSCN/Au	1.48	23.27	83.18	28.66	Simulation	our

performance exhibited an inverse relationship with defect density, while it almost exhibited a proportional relationship with the doping density. Fundamentally, the strong built-in electric field, high conductivity and low electron-hole recombination rate caused an improvement in the PV parameters. The optimized solar cell had a 500 nm thick absorber layer with an  $N_A$  of  $1 \times 10^{16} \text{ cm}^{-3}$  and a  $N_t$  of  $2.6 \times 10^{13} \text{ cm}^{-3}$ . The final choice of the doping density of ETL and HTL in the optimized simulation were  $5 \times 10^{20} \text{ cm}^{-3}$  and  $1 \times 10^{20} \text{ cm}^{-3}$ , respectively. In addition, the maximum PCE of 28.66% was achieved at 3.7 eV electron affinity of ETL and 2.1 eV electron affinity of HTL. Furthermore, the proposed solar cell had the best performance at an operation temperature of 300 K. It is believed that such stable PSC may serve as a highly efficient solar cell in future photovoltaic applications.

## Funding

This work is supported by the Foreign Expert Project of Ministry of Science and Technology (NO. DL2023014015 L).

## CRediT authorship contribution statement

**Ting Gou:** Conceptualization, Formal analysis, Methodology, Writing – original draft, Writing – review & editing. **Yang Li:** Formal analysis, Methodology, Resources. **Zeyuan Lv:** Methodology. **Minglin Zhao:** Conceptualization, Funding acquisition, Methodology, Writing – original draft, Writing – review & editing. **Jun Dai:** Funding acquisition, Project administration, Supervision. **Fuyang Cao:** Conceptualization, Writing – review & editing.

## Declaration of competing interest

The authors declare that they have no known competing financial interests or personal relationships that could have appeared to influence the work reported in this paper.

## Data availability

Data will be made available on request.

## References

- [1] J. De Roo, M. Ibáñez, P. Geiregat, et al., Highly dynamic ligand binding and light absorption coefficient of cesium lead bromide perovskite nanocrystals, *ACS Nano* 10 (2) (2016) 2071–2081.
- [2] S.D. Stranks, G.E. Eperon, G. Grancini, et al., Electron-hole diffusion lengths exceeding 1 micrometer in an organometal trihalide perovskite absorber, *Science* 342 (6156) (2013) 341–344.
- [3] E.L. Unger, L. Kegelmann, K. Suchan, et al., Roadmap and roadblocks for the band gap tunability of metal halide perovskites, *J. Mater. Chem. A* 5 (23) (2017) 11401–11409.
- [4] T. Liu, W. Tang, S. Luong, et al., High charge carrier mobility in solution processed one-dimensional lead halide perovskite single crystals and their application as photodetectors, *Nanoscale* 12 (17) (2020) 9688–9695.
- [5] A. Kojima, K. Teshima, Y. Shirai, et al., Organometal halide perovskites as visible-light sensitizers for photovoltaic cells, *J. Am. Chem. Soc.* 131 (17) (2009) 6050–6051.
- [6] J. Park, J. Kim, H.S. Yun, et al., Controlled growth of perovskite layers with volatile alkylammonium chlorides, *Nature* 616 (7958) (2023) 724–730.
- [7] Y. Chen, X. Zuo, Y. He, et al., Dual passivation of perovskite and  $\text{SnO}_2$  for high-efficiency  $\text{MAPbI}_3$  perovskite solar cells, *Adv. Sci.* 8 (5) (2021) 2001466.
- [8] R. Lu, Y. Liu, J. Zhang, et al., Highly efficient (200) oriented  $\text{MAPbI}_3$  perovskite solar cells, *Chem. Eng. J.* 433 (2022) 133845.
- [9] M.K. Sardashti, M. Zendehdel, N.Y. Nia, et al., High efficiency  $\text{MAPbI}_3$  perovskite solar cell using a pure thin film of polyoxometalate as scaffold layer, *ChemSusChem* 10 (19) (2017) 3773–3779.
- [10] Y.M. Xie, C. Ma, X. Xu, et al., Revealing the crystallization process and realizing uniform 1.8 eV MA-based wide-bandgap mixed-halide perovskites via solution engineering, *Nano Res.* 12 (2019) 1033–1039.
- [11] A.F. Akbulatov, M.I. Ustinova, G.V. Shilov, et al., Temperature dynamics of  $\text{MAPbI}_3$  and  $\text{PbI}_2$  photolysis: revealing the interplay between light and heat, two enemies of perovskite photovoltaics, *J. Phys. Chem. Lett.* 12 (18) (2021) 4362–4367.
- [12] G.E. Eperon, S.D. Stranks, C. Menelaou, et al., Formamidinium lead trihalide: a broadly tunable perovskite for efficient planar heterojunction solar cells, *Energy Environ. Sci.* 7 (3) (2014) 982–988.
- [13] X. Zheng, C. Wu, S.K. Jha, et al., Improved phase stability of formamidinium lead triiodide perovskite by strain relaxation, *ACS Energy Lett.* 1 (5) (2016) 1014–1020.
- [14] S. Bai, P. Da, C. Li, et al., Planar perovskite solar cells with long-term stability using ionic liquid additives, *Nature* 571 (7764) (2019) 245–250.
- [15] S. Asmontas, A. Čerškus, J. Gradauskas, et al., Impact of cesium concentration on optoelectronic properties of metal halide perovskites, *J. Mater.* 15 (5) (2022) 1936.
- [16] A.M. El-Naggar, M.M. Osman, A.Q. Alanaizi, et al., Spectroscopic ellipsometry and solar cell performance of  $\text{Cs-doped MA}_{0.05}\text{FA}_{0.95}\text{Pb(I}_{0.98}\text{Br}_{0.02}\text{)}_3$  triple cation perovskite thin films for solar cell applications, *Appl. Phys. A* 128 (5) (2022) 378.
- [17] M. Azam, S. Yue, R. Xu, et al., Highly efficient solar cells based on Cl incorporated tri-cation perovskite materials, *J. Mater. Chem. A* 6 (28) (2018) 13725–13734.
- [18] A.K. Jena, A. Kulkarni, T. Miyasaka, Halide perovskite photovoltaics: background, status, and future prospects, *Chem. Rev.* 119 (5) (2019) 3036–3103.
- [19] W. Zhang, L. Huang, W. Zheng, et al., Revealing key factors of efficient narrow-bandgap mixed lead-tin perovskite solar cells via numerical simulations and experiments, *Nano Energy* 96 (2022) 107078.
- [20] S. Mushtaq, S. Tahir, A. Ashfaq, et al., Performance optimization of lead-free  $\text{MASnBr}_3$  based perovskite solar cells by SCAPS-1D device simulation, *Sol. Energy* 249 (2023) 401–413.
- [21] H. Sabbah, J. Arayro, R. Mezher, Numerical simulation and optimization of highly stable and efficient lead-free perovskite  $\text{FA}_{1-x}\text{Cs}_x\text{SnI}_3$ -based solar cells using SCAPS, *Materials* 15 (14) (2022) 4761.
- [22] E. Raza, Z. Ahmad, F. Aziz, et al., Numerical simulation analysis towards the effect of charge transport layers electrical properties on cesium based ternary cation perovskite solar cells performance, *Sol. Energy* 225 (2021) 842–850.

- [23] B. Mahapatra, R.V. Krishna, P.K. Patel, Design and optimization of CuSCN/CH<sub>3</sub>NH<sub>3</sub>PbI<sub>3</sub>/TiO<sub>2</sub> perovskite solar cell for efficient performance, *Opt Commun.* 504 (2022) 127496.
- [24] A.R. Kirmani, B.K. Durant, J. Grandidier, et al., Countdown to perovskite space launch: guidelines to performing relevant radiation-hardness experiments, *Joule* 6 (5) (2022) 1015–1031.
- [25] L. Zheng, Y.H. Chung, Y. Ma, et al., A hydrophobic hole transporting oligothiophene for planar perovskite solar cells with improved stability, *Chem. Commun.* 50 (76) (2014) 11196–11199.
- [26] P. Pattanasattayavong, N. Yaacobi-Gross, K. Zhao, et al., Hole-transporting transistors and circuits based on the transparent inorganic semiconductor copper (I) thiocyanate (CuSCN) processed from solution at room temperature, *Adv. Mater.* 25 (10) (2013) 1504–1509.
- [27] M. Jung, Y.C. Kim, N.J. Jeon, et al., Thermal stability of CuSCN hole conductor-based perovskite solar cells, *ChemSusChem* 9 (18) (2016) 2592–2596.
- [28] S. Ye, W. Sun, Y. Li, et al., CuSCN-based inverted planar perovskite solar cell with an average PCE of 15.6%, *Nano Lett.* 15 (6) (2015) 3723–3728.
- [29] J.W. Jung, C.C. Chueh, A.K.Y. Jen, High-performance semitransparent perovskite solar cells with 10% power conversion efficiency and 25% average visible transmittance based on transparent CuSCN as the hole-transporting material, *Adv. Energy Mater.* 5 (17) (2015) 1500486.
- [30] J. Choi, S. Song, M.T. Horantner, et al., Well-Defined Nanostructured, Single-crystalline TiO<sub>2</sub> electron transport layer for efficient planar perovskite solar cells, *ACS Nano* 10 (6) (2016) 6029–6036.
- [31] M.M. Tavakoli, P. Yadav, R. Tavakoli, et al., Surface engineering of TiO<sub>2</sub> ETL for highly efficient and hysteresis-less planar perovskite solar cell (21.4%) with enhanced open-circuit voltage and stability, *Adv. Energy Mater.* 8 (23) (2018) 1800794.
- [32] J. Madan, R. Pandey, R. Sharma, Device simulation of 17.3% efficient lead-free all-perovskite tandem solar cell, *Sol. Energy* 197 (2020) 212–221.
- [33] T. Minemoto, Y. Kawano, T. Nishimura, et al., Numerical reproduction of a perovskite solar cell by device simulation considering band gap grading[J, Opt. Mater. 92 (2019) 60–66.
- [34] H.J. Du, W.C. Wang, J.Z. Zhu, Device simulation of lead-free CH<sub>3</sub>NH<sub>3</sub>SnI<sub>3</sub> perovskite solar cells with high efficiency, *Chin. Phys. B* 25 (10) (2016) 108802.
- [35] M. Anaya, J.P. Correa-Baena, G. Lozano, et al., Optical analysis of CH<sub>3</sub>NH<sub>3</sub>Sn<sub>x</sub>Pb<sub>1-x</sub>I<sub>3</sub> absorbers: a roadmap for perovskite-on-perovskite tandem solar cells, *J. Mater. Chem. A* 4 (29) (2016) 11214–11221.
- [36] S.A. Rutledge, A.S. Helmy, Carrier mobility enhancement in poly (3,4-ethylenedioxithiophene)-poly (styrenesulfonate) having undergone rapid thermal annealing, *J. Appl. Phys.* 114 (13) (2013).
- [37] S. Bansal, P. Aryal, Evaluation of New Materials for Electron and Hole Transport Layers in Perovskite-Based Solar Cells through SCAPS-1D simulations[C]// 2016 IEEE 43rd Photovoltaic Specialists Conference (PVSC), IEEE, 2016, pp. 747–750.
- [38] N. Arora, M.I. Dar, A. Hinderhofer, et al., Perovskite solar cells with CuSCN hole extraction layers yield stabilized efficiencies greater than 20%, *Science* 358 (6364) (2017) 768–771.
- [39] J. Euvrard, Y. Yan, D.B. Mitzi, Electrical doping in halide perovskites, *Nat. Rev. Mater.* 6 (6) (2021) 531–549.
- [40] A. Bag, R. Radhakrishnan, R. Nekovei, et al., Effect of absorber layer, hole transport layer thicknesses, and its doping density on the performance of perovskite solar cells by device simulation, *Sol. Energy* 196 (2020) 177–182.
- [41] P.K. Patel, Device simulation of highly efficient eco-friendly CH<sub>3</sub>NH<sub>3</sub>SnI<sub>3</sub> perovskite solar cell, *Sci. Rep.* 11 (1) (2021) 3082.
- [42] H. Bencherif, F. Meddour, M.H. Elshorbagy, et al., Performance enhancement of (FAPbI<sub>3</sub>)<sub>1-x</sub>(MAPbBr<sub>3</sub>)<sub>x</sub> perovskite solar cell with an optimized design, *J. Micro and Nanostructures* 171 (2022) 207403.
- [43] M.K. Hossain, G.F.I. Toki, A. Kuddus, et al., An extensive study on multiple ETL and HTL layers to design and simulation of high-performance lead-free CsSnCl<sub>3</sub>-based perovskite solar cells, *Sci. Rep.* 13 (1) (2023) 2521.
- [44] M.K. Hossain, D.P. Samajdar, R.C. Das, et al., Design and simulation of Cs<sub>2</sub>BiAgI<sub>6</sub> double perovskite solar cells with different electron transport layers for efficiency enhancement, *Energy & Fuels* 37 (5) (2023) 3957–3979.
- [45] M.K. Hossain, A.A. Arnab, R.C. Das, et al., Combined DFT, SCAPS-1D, and wxAMPS frameworks for design optimization of efficient Cs<sub>2</sub>BiAgI<sub>6</sub>-based perovskite solar cells with different charge transport layers, *RSC advances* 12 (54) (2022) 35002–35025.
- [46] M. Lazemi, S. Asgharizadeh, S. Bellucci, A computational approach to interface engineering of lead-free CH<sub>3</sub>NH<sub>3</sub>SnI<sub>3</sub> highly-efficient perovskite solar cells, *Phys. Chem. Chem. Phys.* 20 (40) (2018) 25683–25692.
- [47] S. Karthick, S. Velumani, J. Bouclé, Chalcogenide BaZrS<sub>3</sub> perovskite solar cells: a numerical simulation and analysis using SCAPS-1D, *Opt. Mater.* 126 (2022) 112250.
- [48] M.S. Chowdhury, S.A. Shahahmadi, P. Chelvanathan, et al., Effect of deep-level defect density of the absorber layer and n/i interface in perovskite solar cells by SCAPS-1D, *Results Phys.* 16 (2020) 102839.
- [49] J. Li, B. Pradhan, S. Gaur, et al., Predictions and strategies learned from machine learning to develop high-performing perovskite solar cells, *Adv. Energy Mater.* 9 (46) (2019) 1901891.
- [50] X. Meng, T. Tang, R. Zhang, et al., Optimization of germanium-based perovskite solar cells by SCAPS simulation, *Opt. Mater.* 128 (2022) 112427.
- [51] L. Hao, M. Zhou, Y. Song, et al., Tin-based perovskite solar cells: further improve the performance of the electron transport layer-free structure by device simulation, *Sol. Energy* 230 (2021) 345–354.
- [52] L. Calíó, S. Kazim, M. Grätzel, et al., Hole-transport materials for perovskite solar cells, *Angew. Chem. Int. Ed.* 55 (47) (2016) 14522–14545.
- [53] S. Abdelaziz, A. Zekry, A. Shaker, et al., Investigating the performance of formamidinium tin-based perovskite solar cell by SCAPS device simulation, *Opt. Mater.* 101 (2020) 109738.
- [54] T. Minemoto, M. Murata, Theoretical analysis on effect of band offsets in perovskite solar cells, *Sol. Energy Mater. Sol. Cell.* 133 (2015) 8–14.
- [55] N. Singh, A. Agarwal, M. Agarwal, Study the effect of band offsets on the performance of lead-free double perovskite solar cell, *Opt. Mater.* 125 (2022) 112112.
- [56] N. Singh, A. Agarwal, M. Agarwal, Study the effect of band offsets on the performance of lead-free double perovskite solar cell, *Opt. Mater.* 125 (2022) 112112.
- [57] D. Prochowicz, M.M. Tavakoli, A. Solanki, et al., Understanding the effect of chlorobenzene and isopropanol anti-solvent treatments on the recombination and interfacial charge accumulation in efficient planar perovskite solar cells, *J. Mater. Chem. A* 6 (29) (2018) 14307–14314.
- [58] V. Sebastian, J. Kurian, Simulation and optimization studies on CsPbI<sub>3</sub> based inorganic perovskite solar cells, *Sol. Energy* 221 (2021) 99–108.
- [59] H. Bencherif, M.K. Hossain, Design and numerical investigation of efficient (FAPbI<sub>3</sub>)<sub>1-x</sub>(CsSnI<sub>3</sub>)<sub>x</sub> perovskite solar cell with optimized performances, *Sol. Energy* 248 (2022) 137–148.
- [60] M.K. Hossain, G.F. Ishraque Toki, D.P. Samajdar, et al., Photovoltaic performance investigation of Cs<sub>3</sub>Bi2I<sub>9</sub>-based perovskite solar cells with various charge transport channels using DFT and SCAPS-1D frameworks, *Energy & Fuels* 37 (10) (2023) 7380–7400.
- [61] M.K. Hossain, G.F.I. Toki, D.P. Samajdar, et al., Deep Insights into the Coupled Optoelectronic and Photovoltaic Analysis of Lead-Free CsSnI<sub>3</sub> Perovskite-Based Solar Cell Using DFT Calculations and SCAPS-1D Simulations[J], ACS Omega, 2023.
- [62] M.F. Rahman, M.J.A. Habib, M.H. Ali, et al., Design and numerical investigation of cadmium telluride (CdTe) and iron silicide (FeSi<sub>2</sub>) based double absorber solar cells to enhance power conversion efficiency, *AIP Adv.* 12 (10) (2022).
- [63] I.M. De Los Santos, H.J. Cortina-Marrero, M.A. Ruiz-Sánchez, et al., Optimization of CH<sub>3</sub>NH<sub>3</sub>PbI<sub>3</sub> perovskite solar cells: a theoretical and experimental study, *Sol. Energy* 199 (2020) 198–205.
- [64] S. Karthick, S. Velumani, J. Bouclé, Experimental and SCAPS simulated formamidinium perovskite solar cells: a comparison of device performance, *Sol. Energy* 205 (2020) 349–357.